ChemPubSoc Europe

DOI: 10.1002/cphc.201701058

CHEMPHYSCHEM Articles

Special Issue

Multi-site Cooperativity in Alkali-Metal-Exchanged Faujasites for the Production of Biomass-Derived Aromatics

Roderigh Y. Rohling,[a] Emiel J. M. Hensen,*[a] and Evgeny A. Pidko*[a, b, c]

The catalytic Diels–Alder cycloaddition–dehydration (DACD) reaction of furanics with ethylene is a promising route to bio-derived aromatics. The reaction can be catalyzed by alkali-metal-exchanged faujasites. Herein, the results of periodic DFT calculations based on accurate structural models of alkali-metal-exchanged zeolites are presented, revealing the fundamental roles that confinement and the nature of the exchangeable cations in zeolite micropores have in the performance of faujasite-based catalysts in the DACD reaction. Special attention is devoted to analyzing the effect of functional substituents on furanic substrates (furan, 2,5-dimethylfuran, 2,5-furandicarboxylic acid) on the catalyst behavior. It is demonstrated that the conventional reactivity theories of the Diels–Alder chemistry based on simplistic single-site Lewis acidity and substituent effects do not apply if catalytic processes in the multiple-site confined environment of zeolite nanopores are considered. The nature and cooperativity of the interactions between the multiple exchangeable cations and the substrates determine the reaction energetics of the elementary steps involved in the DACD process.

1. Introduction

Zeolites are crystalline aluminosilicates containing molecule-sized micropores arranged in a regular manner.[1] They are built from tetrahedral TO_4 building blocks ($T = Si^{4+}$ or Al^{3+}), the spatial arrangement and connectivity of which determine the size and shape of the micropores. The chemical composition of the lattice defines the reactivity of the zeolite matrix. The introduction of Al^{3+} into a neutral siliceous structure generates a negative charge on the framework that needs to be balanced by an extra-framework counter cation. Compensation of the negative charge by protons generates strong Brønsted acid sites inside the zeolite micropores, whereas the introduction of metal cations gives rise to Lewis acidic sites. The rich inorganic chemistry of the extra-framework species located inside the micropores with tunable geometries is key to the widespread and versatile applications of zeolites as selective catalysts for current and emerging chemical processes.[2–4]

Most theories on reactivity in zeolite catalysis are based on shape selectivity imposed on the catalytic reaction by the micropore topology and the intrinsic chemical properties of an individual active site. The former relates activity and selectivity to the geometric fit of the reactive species, intermediates or transition states in the zeolite pores.[5,6] The consideration of zeolites as single-site catalysts facilitates the mechanistic description of the complex chemical processes inside the zeolite micropores. Furthermore, it allows the construction of straightforward structure–activity relationships.[7–11]

Besides the main applications in the petroleum refining industry, zeolites are promising catalysts for the conversion of renewable biomass into chemical intermediates.[12–14] The production of aromatic compounds (e.g., BTX—benzene, toluene and xylenes) from biomass, which are currently produced solely from fossil hydrocarbon resources, is highly desirable.[15,16] Catalytic depolymerization of lignin and lignocellulose is challenging and yields low amounts of substituted aromatics.[17–22] A potentially more selective approach involves the use of (hemi)cellulose as the starting material.[23–26] Hydrolysis of polysaccharides yields glucose, xylose and other sugars,[14] which can then be converted by dehydration[24,26] followed by reduction or oxidation to substituted furans[26] (Figure 1). The Diels–Alder cycloaddition of alkenes to furanic compounds

[a] R. Y. Rohling, Prof. Dr. E. J. M. Hensen, Prof. Dr. E. A. Pidko
Inorganic Materials Chemistry Group, Schuit Institute of Catalysis
Eindhoven University of Technology
P.O. Box 513, 5600 MB
Eindhoven (The Netherlands)
E-mail: e.j.m.hensen@tue.nl

[b] Prof. Dr. E. A. Pidko
TheoMAT group, Laboratory of Solution Chemistry for Advanced Materials and Technologies, ITMO University
Lomonosova 9, St. Petersburg, 191002 (Russia)

[c] Prof. Dr. E. A. Pidko
Current Address: Inorganic Systems Engineering group
Department of Chemical Engineering, Faculty of Applied Sciences
Delft University of Technology
Van der Maasweg 9, 2629 HZ
Delft (The Netherlands)
E-mail: e.a.pidko@tudelft.nl

Supporting Information and the ORCID identification number(s) for the author(s) of this article can be found under: https://doi.org/10.1002/cphc.201701058.

An invited contribution to a Special Issue on Reactions in Confined Spaces

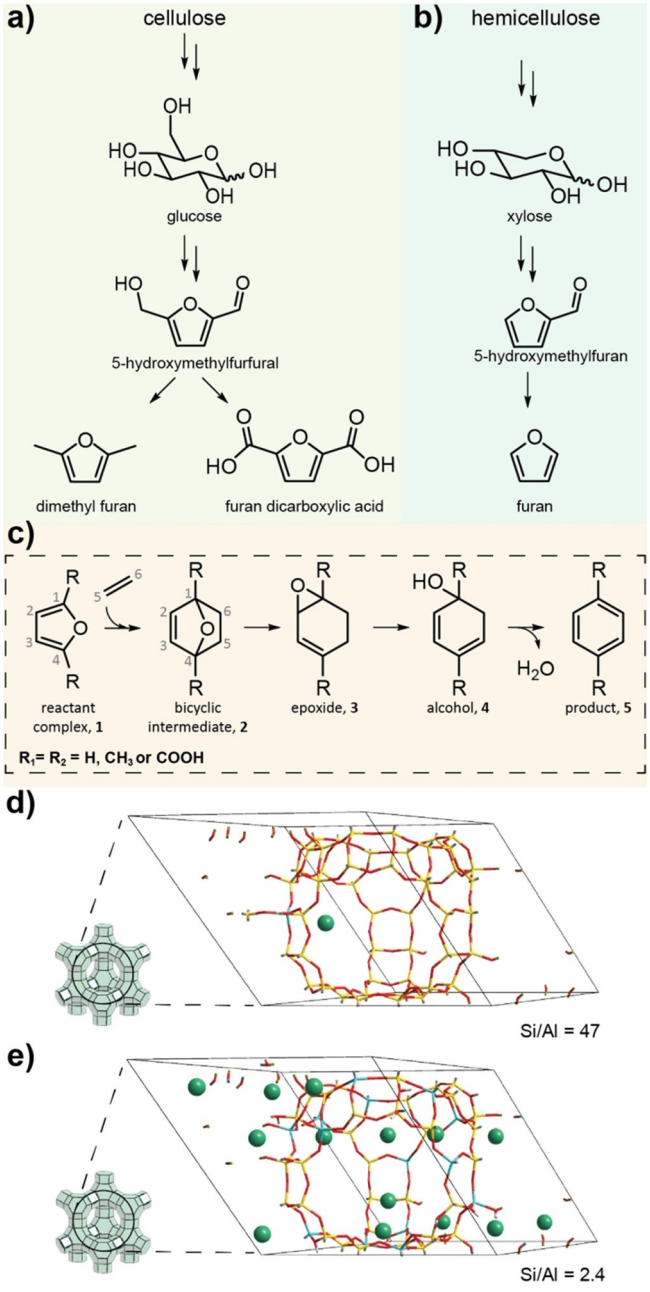

Figure 1. Formation of a) 2,5-dimethylfuran and 2,5-furandicarboxylic acid from cellulose and b) furan from hemicellulose. c) The furanic compounds are coupled with ethylene in the Diels–Alder cycloaddition–dehydration reaction to produce aromatic compounds. The two models used in this work: d) the high-silica alkali-exchanged isolated site model, and e) the low-silica alkali-metal-exchanged faujasite containing multiple active sites in the faujasite supercages.

yields substituted benzenes. The reaction involves substituted 7-oxanorbornene cycloadducts,[27,28] which high ring strain[29,30] renders reactive towards isomerization into an alcohol intermediate that can dehydrate to aromatic products.[27,28] Such a consecutive cycloaddition, isomerization and dehydration process is usually carried out as a one-pot tandem reaction and will here be denoted as the Diels–Alder cycloaddition–dehydration (DACD) reaction.

One of the most important aromatic compounds is *para*-xylene,[31] which is a commodity chemical mainly used for the production of terephthalic acid (TPA).[32] One of the main routes to producing TPA is the oxidation of *para*-xylene to transform the methyl groups into carboxylic acids.[32] If a biomass-based route to TPA by the DACD reaction between 2,5-dimethylfuran (2,5-DMF) and ethylene is followed, the process should involve the reintroduction of the oxygenated moieties, which were originally removed from the sugar-derived 5-hydroxymethylfurfural intermediate. An alternative route to TPA by directly using biomass-derived oxygenated furanic intermediates in a DACD reaction is therefore more appealing and potentially more atom-efficient.[32]

In recent years, many experimental[33–43] and theoretical[44–46] studies have been devoted to the DACD conversion of furanic compounds and alkenes to aromatics over different heterogeneous catalysts. Most studies focused on the DACD reaction of 2,5-DMF with ethylene to produce *para*-xylene. The common catalysts are Brønsted acidic large-pore zeolites such as HY[33,42] and HBEA,[35,44] or Lewis acidic zeolites such as the alkali-metal-exchanged faujasites[46,47] and Sn-, Zr- or Ti-doped beta polymorph A (BEA).[36] The DACD reaction of 2-methylfuran with ethylene over heterogeneous Lewis acid faujasites and homogeneous Lewis acid metal chloride catalysts has been studied by Wijaya et al.[37] Dehydrative aromatization of the cycloadduct originating from the DAC reaction of furanic compounds with ethanol in the presence of Brønsted acidic zeolite catalysts was studied by Tsang et al.[38] and Zhao et al.[39] The DACD conversion of furan and acrylic acid over Hf-, Zr- and Sn-BEA was investigated by Mahmoud et al.[40] The conversion of highly oxygenated furanic compounds with ethylene over Lewis acidic Sn-BEA catalysts towards oxygenated aromatic compounds was originally described by the group of Davis[41] and subsequently investigated in detail by Bell and co-workers.[45] In general, most of the studies reported to date identified Brønsted acids as the preferred catalysts for the DACD conversion of the reduced furanic intermediates, whereas the selective transformation of the oxygenated substrates can be achieved by using strongly Lewis acidic Sn-BEA catalysts, the unique catalytic behavior of which is often related to the active site cooperativity within its micropores.[48–51]

We have recently demonstrated that the DACD reaction between 2,5-DMF and ethylene to produce *para*-xylene can be efficiently carried out using alkali-metal-exchanged faujasite catalysts.[47] Low-silica zeolites containing hard Lewis acid sites were initially regarded as less active catalysts than their Brønsted acid counterparts.[46,52] A combination of periodic DFT calculations with microkinetic modeling revealed that the activity of the catalysts depends strongly on the nature of the exchangeable cations. These findings were supported by parallel kinetic studies, which identified KY zeolite as a superior catalyst for the DACD reaction. Importantly, the DFT calculations showed that the cooperative action of multiple cations in the confined faujasite micropores should be taken into account to explain the activity trends. Clearly, the description of the mechanism using an isolated-site model is too simple.

Herein, we report a computational study on the effect of active-site cooperativity and the nature of the furanic substrate on the DACD reactions of furan, 2,5-DMF and 2,5-furandicarboxylic acid (FDCA) with ethylene to give benzene, *para*-xylene and TPA, respectively, over alkali-exchanged zeolites. To this end, we compared the results of periodic DFT calculations obtained with two distinct alkali-exchanged zeolite models, namely the simplified high-silica FAU isolated site model (Figure 1 d) and the more chemically representative low-silica model of zeolite Y (Figure 1 e).

This article is organized as follows: we introduce a brief overview of the DACD reaction mechanism and the common notations used throughout the paper in Section 2.1. We continue by discussing the results of periodic DFT calculations on the catalytic conversion of furan, 2,5-DMF and FDCA in Sections 2.2, 2.3 and 2.4, respectively. For each substrate, the computational results obtained with the single- and multiple-site models are discussed separately. This is followed by Section 3 in which the summary and key conclusions of this work are given. The computational details are presented in the Experimental Section.

2. Results and Discussion

2.1. Reaction Mechanism

The DACD reaction starts with the co-adsorption of the furanic reactant and ethylene in the alkali-metal (M)-exchanged faujasite catalyst. We analyzed two different models, that we refer to here as MFAU and MY, being M-exchanged faujasite with an isolated site and multiple accessible sites, respectively. Specifically, MFAU refers to the faujasite model with a Si/Al-ratio of 47 and MY is the model with a Si/Al-ratio of 2.4. The adsorbed states are denoted as **1**/MFAU or **1**/MY (e.g., furan $+ C_2H_4 +$ MY $\rightarrow$ **1**/MY). All reaction mechanisms follow a similar sequence of elementary steps (Figure 1 c), which are described below for furan as the representative example. The reaction starts with the Diels–Alder cycloaddition, which proceeds by synchronous coupling of C1 to C6 and C4 to C5. This gives a bicyclic 7-oxabicyclo[2.2.1]hept-2-ene intermediate **2**, which then undergoes two isomerization steps, **2** $\rightarrow$ **3** $\rightarrow$ **4**. In this sequence of elementary steps, the furanic oxygen atom (O_f) adopts a new bridging position between C1 and C2, forming the 7-oxabicyclo[4.1.0]-hept-2-ene epoxide intermediate **3**. Next, abstraction of the methylene C5 proton yields the cyclohexa-2,4-dien-1-ol alcohol species **4**. Finally, dehydration occurs involving an intramolecular proton shift from the C6 atom to the O_fH group, resulting in the formation of the benzene and water (**5** $+ H_2O$). In the subsequent sections the mechanisms of the conversion of each of the furanic substrates by cation-exchanged faujasites will be discussed.

2.2. DACD Reaction of Furan with Ethylene

Furan is the simplest furanic compound lacking functional substituents. The computational results for the reaction of furan with ethylene will serve as a reference onto which we can reflect the data obtained for the other substrates. The energy diagrams for the DACD reaction of furan with ethylene over Na-, K- and Rb-exchanged faujasite models are reported in Figure 2. Figure 2 a and b show the results for the MFAU and MY models, respectively.

2.2.1. Reaction over the MFAU Single-Site Model

The MFAU models contain exchangeable alkali ions, which can be stabilized at different cation positions (SI–SIII, Figure 3).[53] Only two of these are accessible to adsorbents and can therefore be considered active sites. These are 1) the SII position located at the six-membered ring of the sodalite cage, facing the supercage, and 2) the SIII site located at the four-membered rings at the side of the sodalite cage, facing the supercage. An alternative to SIII is the SIII′ site (3), which essentially is a dislocated SIII site, located at the edge of the 12-membered window between two different supercages.

We first determined the preferential adsorption sites for furan and ethylene at both the SII and SIII sites. The computed adsorption energies for the complexes at different cation sites are given in Table S1 in the Supporting Information. To summarize, the differences in adsorption energies of η^5-coordinated furan on the SII and SIII sites are small in all the studied MFAU models. The largest difference was found for NaFAU, favoring the SII adsorption site over SIII by only 6 kJ mol^{-1}. Compared to furan, ethylene adsorption is about 16 and 20 kJ mol^{-1} weaker at SII and SIII, respectively. A maximum difference in ethylene adsorption energies was also found for NaFAU with a slight (9 kJ mol^{-1}) preference for adsorption to the SII cation. However, as the space around the cation at SIII is more open than at SII, we selected SIII as the active site for the DACD reaction of **1**/MFAU models. In the starting geometry, furan is η^5-coordinated to the SIII cation and ethylene is weakly adsorbed to the siliceous walls of the faujasite supercage.

The catalytic cycle begins with the synchronous DAC reaction (**1** $\rightarrow$ **2**) during which two new C–C bonds are formed in concert. This step is exothermic, with computed reaction energies (ΔE) ranging from -66 kJ mol^{-1} for RbFAU to -79 kJ mol^{-1} for NaFAU. The DAC barriers are the highest for KFAU and RbFAU (63 kJ mol^{-1}) and the lowest for NaFAU (58 kJ mol^{-1}). The increase of the reaction enthalpies with a concomitant decrease of the activation barriers is consistent with the decrease of the Lewis acidity of the cations as a function of ionic radius from Na^+ to Rb^+. The maximal deviation in the lengths of the C1–C6 and C4–C5 bonds that are formed, is approximately 0.01 Å for **TS1**/KFAU.

In the next two steps of epoxide (**2** $\rightarrow$ **3**) and alcohol formation (**3** $\rightarrow$ **4**), the electronegative O_f atom remains coordinated to the cation, allowing for efficient stabilization of the reaction intermediates. The epoxide-forming step (**2** $\rightarrow$ **3**) is slightly endothermic (<17 kJ mol^{-1}) and proceeds with somewhat similar barriers for all MFAU models. The highest barrier of 176 kJ mol^{-1} was computed for RbFAU, which is only 8 kJ mol^{-1} higher than the lowest value predicted for NaFAU (168 kJ mol^{-1}). The system is stabilized at the second isomerization step involving an intermolecular proton shift to form the

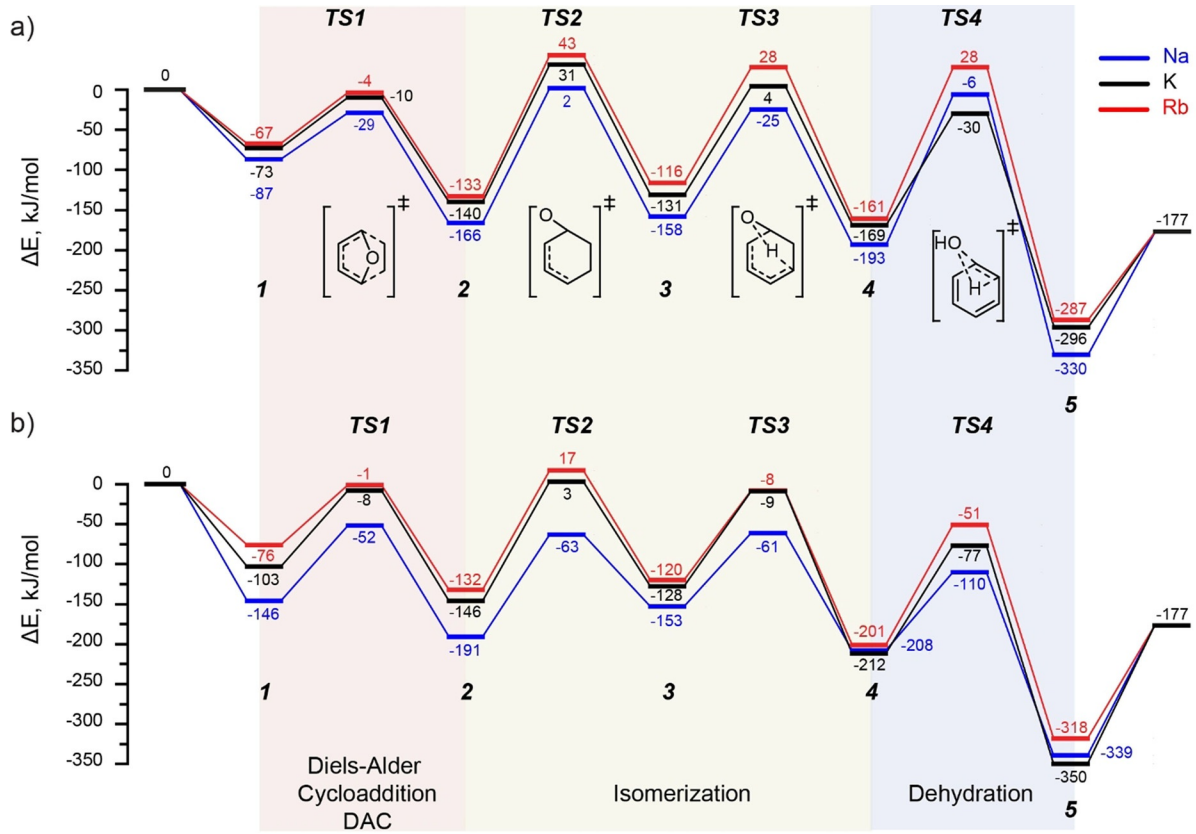

Figure 2. Energy diagrams of the DACD reaction of furan with ethylene yielding benzene, obtained with the periodic DFT calculations over a) the MFAU models and b) the MY models.

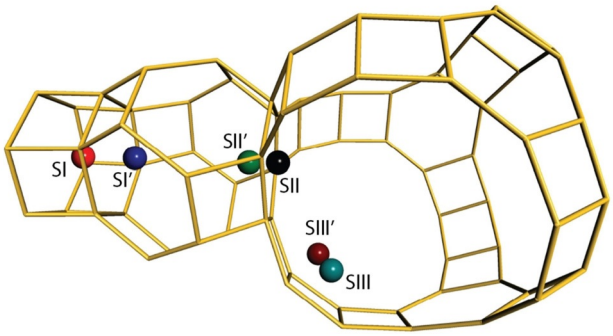

Figure 3. The FAU zeolite structure in which the accessible SII, SIII and SIII′ sites are shown. Sites inaccessible to the reactants are SI, SI′, and SII′.

alcohol intermediate (**3**→**4**). It is most exothermic for RbFAU (−45 kJ mol^{-1}) and least exothermic for NaFAU (−35 kJ mol^{-1}). The barriers for this step range from 133 to 144 kJ mol^{-1}. The barrier increases with decreasing Lewis acidity of the exchangeable cation.

The final dehydration step (**4**→**5**) provides the major thermodynamic driving force for the overall process. The reaction takes place through the intramolecular hydrogen transfer from C6 to the O_fH group coordinated to the exchangeable cation. This reaction is strongly exothermic and characterized by similar enthalpies computed for both KFAU and RbFAU (−126 and −127 kJ mol^{-1}, respectively), and −137 kJ mol^{-1} for NaFAU. The dehydration activation energy is the highest (189 kJ mol^{-1}) for RbFAU and NaFAU (187 kJ mol^{-1}). The reaction over KFAU has a lower barrier of only 139 kJ mol^{-1}. The lower activation barrier leading to **TS4**/KFAU can be rationalized by an analysis of the geometric features of the optimized structures. In **TS4**/KFAU the proton of the O_fH group points away from the zeolite walls into the supercage, whereas it forms a hydrogen bond with the framework oxygen atoms in NaFAU and RbFAU. This hampers molecular reorganization in the transition state, resulting in an increased barrier for the reaction in NaFAU and RbFAU. In addition, in **TS4**/KFAU the benzene-like moiety is tilted upwards with one side (the side of C4/C5, Figure 1c) more so than in either NaFAU or RbFAU. The increased tilting angle is caused by the combination of framework curvature and the size of the potassium cation: in NaFAU the Na^+ ion is too small, such that the dispersive interactions with the matrix are not as strong, whereas the Rb^+ ion is too large, such that insufficient space is available to optimally tilt the benzene moiety for a proper fit. Because we account for dispersive interactions in our work, we rationalized that the geometrical features in KFAU are optimal for providing the most efficient stabilization to **TS4** as compared to NaFAU and RbFAU. To ensure the validity of **TS4**/KFAU, alternative reaction channels including those found for NaFAU and RbFAU were explicitly considered in the calculations. Similarly, multiple reaction

paths were initially tested for NaFAU and RbFAU. All these attempts failed to identify alternative reaction pathways to those discussed here.

At the end of the reaction cycle, the products desorb with activation barriers of 153, 119 and 110 kJ mol^{-1} for NaFAU, KFAU and RbFAU, respectively.

In summary, NaFAU generally interacts with the reactive intermediates more strongly than KFAU or RbFAU. As a consequence, the relative stabilities of the intermediates and transition states are higher for NaFAU. The height of the reaction barriers generally follows the Lewis acidity for the exchangeable cations that trends opposite with the ionic radii. The computed energy profiles indicate the isomerization and dehydration steps to be the rate-limiting elementary steps with the initial DAC reaction only being of minor relevance to the overall performance, which is consistent with the earlier computational findings on cluster models.[52]

2.2.2. Reactions over MY Models

The higher density of cations in MY models results in a large number of possible adsorption and co-adsorption geometries compared to the isolated-site model. The low-silica zeolite provides a reaction environment created by triads of the exchangeable cations at the SII, SIII and the opposite SII site. If furan adopts an η^5-coordination to the SII cation (SII_F) it can simultaneously coordinate to the vicinal SIII site ($SIII_F$) through O_f. Such dual-site adsorption of furan leaves a neighboring SII site accessible for ethylene (SII_{C2}).

We analyzed the different possible adsorption configurations and the main results are summarized in Table S2. The furan adsorption energies on either SII_F or $SIII_F$ differ by only a few kJ mol^{-1}. The greatest difference of only 7 kJ mol^{-1} is observed for RbY, favoring the $SIII_F$ configuration. Because these differences are small, we selected SII as the adsorption site for furan. The adjacent SII site was chosen as the adsorption site for ethylene.

In the low-silica MY models, the DAC reaction (**1**→**2**) starts with ethylene desorption from SII_{C2} to approach furan, followed by a synchronous concerted cycloaddition. The DAC step is least exothermic for KY (−43 kJ mol^{-1}) and most exothermic for RbY (−56 kJ mol^{-1}). The DAC activation energies are 94, 95 and 75 kJ mol^{-1} for Na, K and RbY, respectively. These barriers are higher than those obtained with the MFAU model. Furthermore, their qualitative trend is the reverse of that of the expected cation Lewis acidity. During the reaction, the furan moiety remains coordinated to SII_F with O_f coordinated to the vicinal SIII site. This interaction is so strong that the SIII cation is displaced towards the SII site.

The formation of epoxide **3** is most endothermic on NaY (38 kJ mol^{-1}) and least endothermic on RbY (12 kJ mol^{-1}). The activation energy is the lowest for NaY (128 kJ mol^{-1}) and the highest for KY and RbY (149 kJ mol^{-1} for both catalysts). During this transformation, the interatomic distances $SII_F\cdots O_f$ and $SIII_F\cdots O_f$ become increasingly similar, that is, 2.22 and 2.31 Å for NaY and 2.92 and 2.85 Å for RbY, respectively (Figure 4).

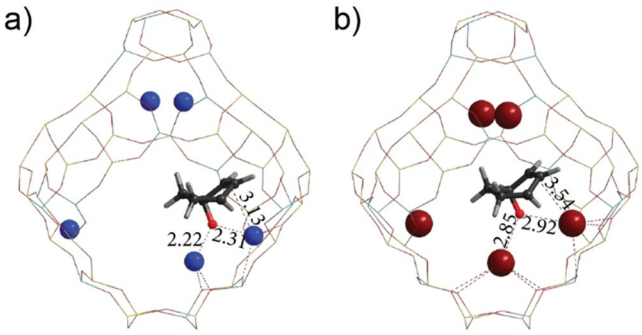

Figure 4. The optimized structures of a) **TS2**/NaY and b) **TS2**/RbY. Selected interatomic distances are expressed in Å.

Next, the isomerization of the epoxide into the alcohol (**3**→**4**) occurs. During this step, the largest energy gains were found for KY and RbY (−84 and −81 kJ mol^{-1}, respectively) and the smallest energy gain was predicted for NaY (−55 kJ mol^{-1}). The activation energy, however, is the smallest for NaY (92 kJ mol^{-1}) and the highest for KY (119 kJ mol^{-1}). For KY and RbY, this step is accompanied by the migration of K^+ and Rb^+ ions to the SIII′ position located at the edge of the four-membered ring. From that position, the cation interacts with the alcohol functional group (2.24 Å for NaY, 2.88 Å for RbY). Such a cation dislocation allows a hydrogen bond to be formed between the OH group and an oxygen atom of the basic framework (the hydrogen bond length is 2.98, 2.91 and 2.71 Å in NaY, KY, and RbY, respectively). Because of this additional stabilization, the relative energies of **4**/KY and **4**/RbY approach that of **4**/NaY (Figure 2). Similarly, **TS2**/MY and **TS3**/MY become substantially stabilized compared to **TS2**/MFAU and **TS3**/MFAU, respectively. This stabilization is least pronounced for **TS3**/KY (13 kJ mol^{-1}), and most for **TS2**/NaY (65 kJ mol^{-1}). Our calculations show that the multiple-site interactions enabled by the MY models give rise to the lower barriers of both isomerization steps relative to those found for the MFAU models. The reaction barrier is least reduced for **3**→**4** in KY ($\Delta\Delta E_{act} = \Delta E_{act,MFAU} - \Delta E_{act,MY} = 16$ kJ mol^{-1}) and most for **3**→**4** in NaY ($\Delta\Delta E_{act} = 41$ kJ mol^{-1}). Despite these quantitative differences, the overall reactivity trends for both structural models are similar and consistent with the Lewis acidity of the cations.

The last dehydration step (**4**→**5**) over MY is assisted by the extra-framework cations, which stabilize the leaving $OH^{\delta-}$ that remains hydrogen-bonded with the zeolite lattice. After the reaction is complete, water remains strongly bound to the cations. The dehydration step is strongly exothermic ($\Delta E > -117$ kJ mol^{-1}) and proceeds with activation barriers of 98, 135 and 150 kJ mol^{-1} for NaY, KY, and RbY, respectively. These barriers have been reduced by 89, 4 and 39 kJ mol^{-1} compared to those found in the MFAU models. To conclude the catalytic cycle, products desorb after overcoming barriers of 162, 173 and 141 kJ mol^{-1}, respectively. These desorption barriers are 9–54 kJ mol^{-1} higher than for the MFAU models.

These results demonstrate that the presence of multiple accessible cation sites strongly affects the reaction energetics of the one-pot DACD reaction of furan with ethylene. Firstly, the

DAC reactivity trend becomes reversed. Whereas the DAC reactivity over the single-site models decreases with increasing ionic radii of the extra-framework cations, the activity of the multiple-site models increases as RbY < NaY < KY. The isomerization and dehydration barriers are also lowered as the result of the additional interactions in the multiple-site environment. However, because the SII–O_f and SIII–O_f interactions are the only significant interactions in the entire network of intermolecular interactions, the reactivity trend predicted for furan with MY models still generally follows the Lewis acidity of the exchangeable cations.

2.3. DACD Reaction of 2,5-DMF with Ethylene

Next, we computationally analyzed the DACD reaction of 2,5-DMF with ethylene to produce *para*-xylene over MFAU and MY zeolite models. The DFT-computed reaction energy diagrams are presented in Figure 5.

2.3.1. Reaction over MFAU Models

2,5-DMF adsorbs almost twice as strong as ethylene, in contrast to furan, the adsorption of which is just slightly stronger than that of ethylene (Table S1). The preferred 2,5-DMF adsorption geometry resembles that of furan with a η^5-coordination mode to the exchangeable cation. The catalytic reaction therefore starts with the coupling of 2,5-DMF adsorbed on the cation and ethylene physisorbed in the supercage (**11**/MFAU). The computed energies of the single 2,5-DMF adsorption as well as 2,5-DMF and ethylene co-adsorption correlate well with the expected Lewis acidity of the exchangeable cations.

At the start of the reaction cycle, the co-adsorbed reactants undergo a DAC reaction (**11**→**12**). The overall reaction enthalpy for **11**→**12** varies from −47 kJ mol^{-1} for KFAU to −68 kJ mol^{-1} for NaFAU. The highest reaction barrier was found for KFAU (88 kJ mol^{-1}) and the lowest for NaFAU (65 kJ mol^{-1}). Although one might expect lower barriers for the DAC reaction of 2,5-DMF with ethylene due to the presence of the two electron-donating methyl substituents in the diene reactant, the calculations show the opposite. For all MFAU models, the computed barriers are approximately 20 kJ mol^{-1} higher for 2,5-DMF compared to furan. We attribute this to the steric repulsion between the alkene and the CH_3 groups of 2,5-DMF hindering the access to the diene moiety of the reactant.

In the next step, the formation of the epoxide **13** (**12**→**13**) through the migration of O_f is aided by the extra-framework cation. This reaction is much less favored than the preceding DAC reaction. The calculated barriers are the lowest for NaFAU

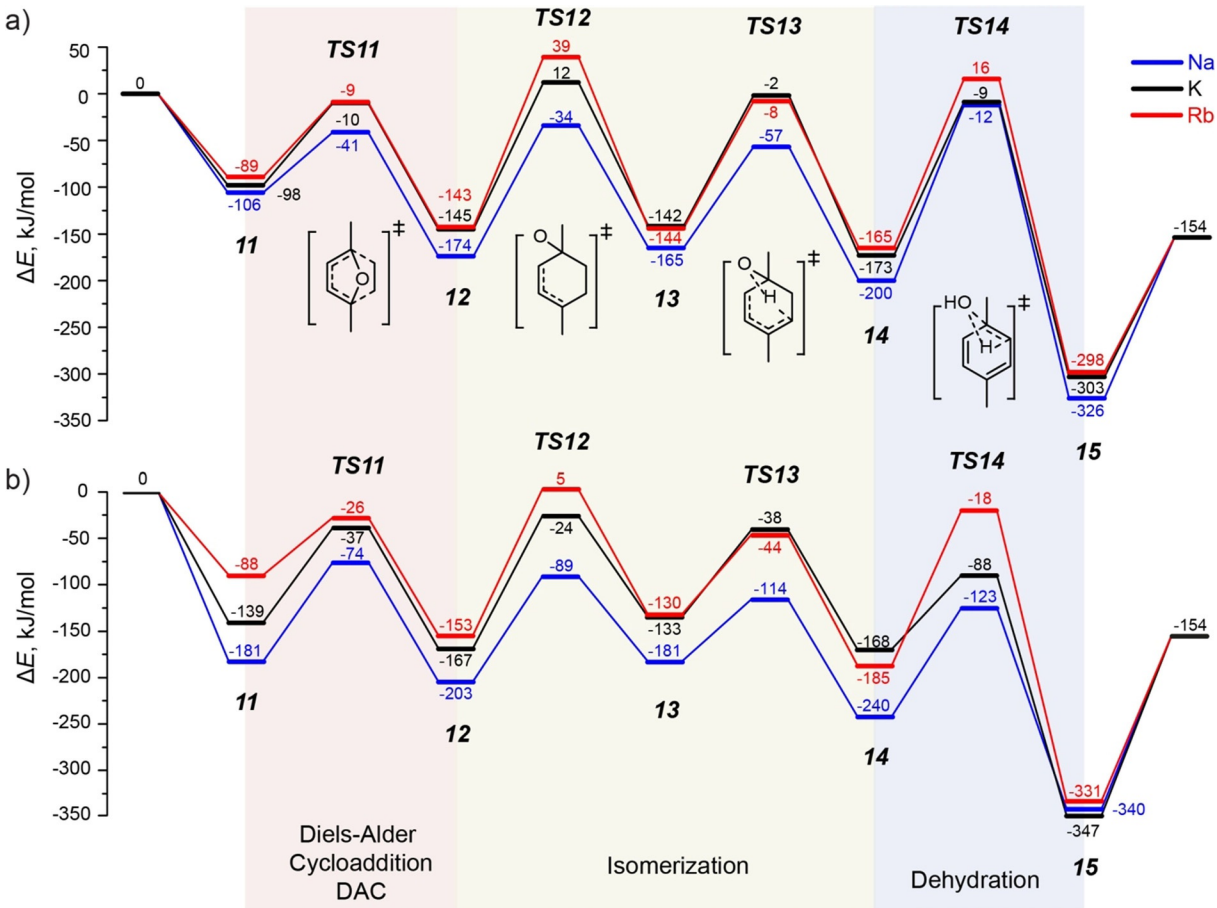

Figure 5. Energy diagrams of the DACD reaction of 2,5-DMF with ethylene yielding *para*-xylene, obtained with the periodic DFT calculations over a) the MFAU models and (b) the MY models.

(140 kJ mol^{-1}) and the highest for RbFAU (182 kJ mol^{-1}). Relative to the reaction **2**→**3**, the formation of epoxide **13** (**12**→**13**) occurs with a 28 and 14 kJ mol^{-1} lower barrier for NaFAU and KFAU, respectively. For RbFAU we found a slightly higher barrier (6 kJ mol^{-1}). Furthermore, **TS12** is 36, 19 and 4 kJ mol^{-1} better stabilized than **TS2** in NaFAU, KFAU and RbFAU, respectively. The generally increased stability of the reaction intermediates and transition states is attributed to the additional van der Waals interactions between the methyl groups of 2,5-DMF and the siliceous zeolite matrix. In RbY, however, the large Rb^+ cation avoids such dispersive interactions between the CH_3 substituents and the zeolite framework.

The formation of alcohol **14** from **13** is slightly exothermic and has barriers of 108, 140 and 136 kJ mol^{-1} in the NaFAU, KFAU and RbFAU models, respectively. Only in NaFAU did we find a reduction of the reaction barrier (15 kJ mol^{-1}) compared to the case of furan conversion. Dispersive interactions additionally stabilize the more bulky **14**/MFAU intermediate by approximately 37 to 57 kJ mol^{-1} compared to **4**/MFAU.

The final dehydration step (**14**→**15**) is only promoted by the electrostatic interaction with a single cation and weak hydrogen-bonding interactions with the siliceous framework. Consequently, the dehydration step (**14**→**15** + H_2O) is highly activated. The computed activation barrier is the largest for NaFAU (188 kJ mol^{-1}) and the smallest for KFAU (164 kJ mol^{-1}). Nevertheless, the overall thermodynamics of the dehydration step is highly favorable and it barely depends on the nature of the exchangeable cation ($\Delta E = -126$ to -133 kJ mol^{-1}). In contrast to the preceding isomerization reactions, the dehydration reaction **14**→**15** does not show major deviations from the energetics computed for **4**→**5** in the high-silica zeolite models. The only significant difference was found for KFAU ($\Delta\Delta E_{act} = +25$ kJ mol^{-1}). Geometry analysis indicates that **TS4**/KFAU is tilted such that it docks onto the curved zeolite framework above the active site, which the methyl groups avoid in **TS14**/KFAU, thus reducing the overall stability of the adsorption complex.

Desorption of the products **15**/MFAU closes the reaction cycle, with barriers of 172, 149 and 144 kJ mol^{-1} for NaFAU, KFAU and RbFAU, respectively. These barriers are 19–34 kJ mol^{-1} higher than for those of **5**/MFAU.

Thus, calculations revealed the epoxide formation and dehydration reaction to be the most likely rate-limiting steps in the overall DACD reaction of 2,5-DMF with ethylene over MFAU-type catalysts. Similar to furan coupling, the initial DAC reaction step appears to be less important for the conversion of 2,5-DMF under the assumption of the single-site nature of faujasite catalysts. In general, the stability of reaction intermediates and transition states increases due to the presence of the methyl group as compared to those originating from the DACD reaction of furan with ethylene.

2.3.2. Reaction over MY Models

Screening of the different adsorption modes revealed that 2,5-DMF adsorption on the SII site ($SII_{2,5\text{-}DMF}$) is preferred over adsorption on the SIII site ($SIII_{2,5\text{-}DMF}$) of MY (Table S2). For example, in NaY, 2,5-DMF coordination to the cation at the SII site is 24 kJ mol^{-1} more favorable than to the cation at the SIII site. The starting configuration in **11**/MY thus consists of 2,5-DMF being η^5-coordinated to the SII site and ethylene adsorbed on the opposite SII site (**11**/MY). Similar to the DACD reaction of furan discussed above, the energy of the co-adsorption of both reactants (**11**/MY) follows the general trend of Lewis acidity of the exchangeable cations.

The DAC reaction starting from **11**/MY to form **12**/MY is most exothermic over RbY (-65 kJ mol^{-1}) and the least over NaY (-22 kJ mol^{-1}). The DAC activation barriers are 107, 102 and 62 kJ mol^{-1} for NaY, KY and RbY, respectively. This is an inverted trend as compared to the DAC reaction over the single-site models (NaFAU < RbFAU < KFAU).

The subsequent isomerization resulting in **13**/MY is only slightly endothermic with reaction energies in the range 22–34 kJ mol^{-1}. Nevertheless, the nature of the cation influences the kinetics of this step significantly. The lowest barrier (114 kJ mol^{-1}) for the step **12**→**13** is predicted for zeolite NaY, whereas the reaction over RbY shows the highest barrier of 158 kJ mol^{-1}. Relative to the same reaction with the MFAU catalysts, the reaction barriers are lower, for example, $\Delta\Delta E_{act}$ is 26 and 14 kJ mol^{-1} for NaY and KY, respectively.

The second isomerization step (**13**→**14**) is exothermic for all models with the most negative energy change found for NaY (-59 kJ mol^{-1}) and the least for KY (-35 kJ mol^{-1}). Note, that in the case of RbY this elementary reaction shows similar exothermicity to that over NaY (-55 kJ mol^{-1}). The computed barriers for the step **13**→**14** were 67, 95 and 86 kJ mol^{-1} for NaY, KY and RbY, respectively. These barriers are lower by approximately 40–50 kJ mol^{-1} compared to those found in the MFAU models. The relative stability of **TS13** also increased, with $\Delta\Delta E_{TS13}$ of approximately 36 to 57 kJ mol^{-1}.

Finally, *para*-xylene and water (**15** + H_2O) are obtained through a highly exothermic dehydration step proceeding with ΔE ranging from -100 kJ mol^{-1} (NaY) to -179 kJ mol^{-1} (KY). For this particular step, the activation barrier is lowest for KY (80 kJ mol^{-1}) and highest for RbY (167 kJ mol^{-1}) with an intermediate value predicted for NaY (117 kJ mol^{-1}). Significantly, these barriers are 71, 84 and 4 kJ mol^{-1} lower than in NaFAU, KFAU and RbFAU, respectively. This is solely attributed to the selective stabilization of the polarized transition state by the multiple-site interactions ($\Delta\Delta E_{TS14} = 111$, 79 and 34 kJ mol^{-1} for NaY, KY and RbY, respectively). The desorption of the products in **15**/MY occurs with barriers of 186, 193 and 177 kJ mol^{-1} for NaY, KY and RbY, respectively. These barriers are higher as compared to those for **5**/MY ($\approx$20–40 kJ mol^{-1}) and **15**/MFAU (14–44 kJ mol^{-1}).

A generalized comparison of the energetics of the one-pot DACD reaction predicted for the coupling of ethylene with 2,5-DMF or furan indicated that the stability of reaction intermediates and transition states increases with the increasing bulkiness of the substrate. Our results point to a positive contribution of attractive dispersive forces between the methyl groups of 2,5-DMF and the zeolite framework.

The presence of multiple active sites and the methyl groups of 2,5-DMF causes significant changes to the qualitative trends

in the computed DAC reaction energetics. The presence of multiple reactive sites allows more efficient stabilization of reaction intermediates and effectively reduces the activation barriers for the elementary steps. A particularly strong stabilizing effect is predicted for the dehydration step over KY. The two methyl groups consistently add 20–30 kJ mol^{-1} to the interaction energy, causing increased stabilization of the reaction intermediates and transition states compared to the same reaction cycle based on the one-pot DACD reaction between furan and ethylene.

2.4. DACD Reaction of FDCA with Ethylene

Finally, we computationally analyzed the reaction energetics of the one-pot DACD reaction of FDCA with ethylene. FDCA contains more-reactive functional groups than furan or 2,5-DMF, that is, COOH moieties. These functional groups are considered electron-withdrawing substituents, suggesting the lower reactivity of the diene in DAC-type reactions. Additionally, the presence of electronegative carboxylate functionalities next to the furanic oxygen atom (O_f) allows the formation of chelating interactions with the exchangeable cations and the formation of additional hydrogen-bonding interactions with the zeolite lattice. Although from an experimental perspective FDCA is not a preferred reagent in view of its low solubility in common solvents,[54] it represents an interesting case study in the context of this article. The results of our periodic DFT calculations on the DACD conversion of FDCA and ethylene are summarized in Figure 6. Selected geometries of different models, discussed throughout the text, are shown in Figures 7 and 8.

2.4.1. Reaction over MFAU Models

The presence of the reactive COOH moieties increases the number of possible adsorption geometries on the cation, even in the case of MFAU. For consistency we limited ourselves to considering the SIII site as the reactive site, as with furan and 2,5-DMF. Nevertheless, even for the SIII adsorption site, three plausible adsorption geometries can be obtained (Figure S1). Two of them involve η^2-coordination of FDCA to the cation via O_f and one of the carbonyl atoms. One of these bidentate geometries also involves a hydrogen bond to a basic framework atom close to the Al substitution. The third mode is η^5-coordinated FDCA, similar to furan or 2,5-DMF. The most stable con-

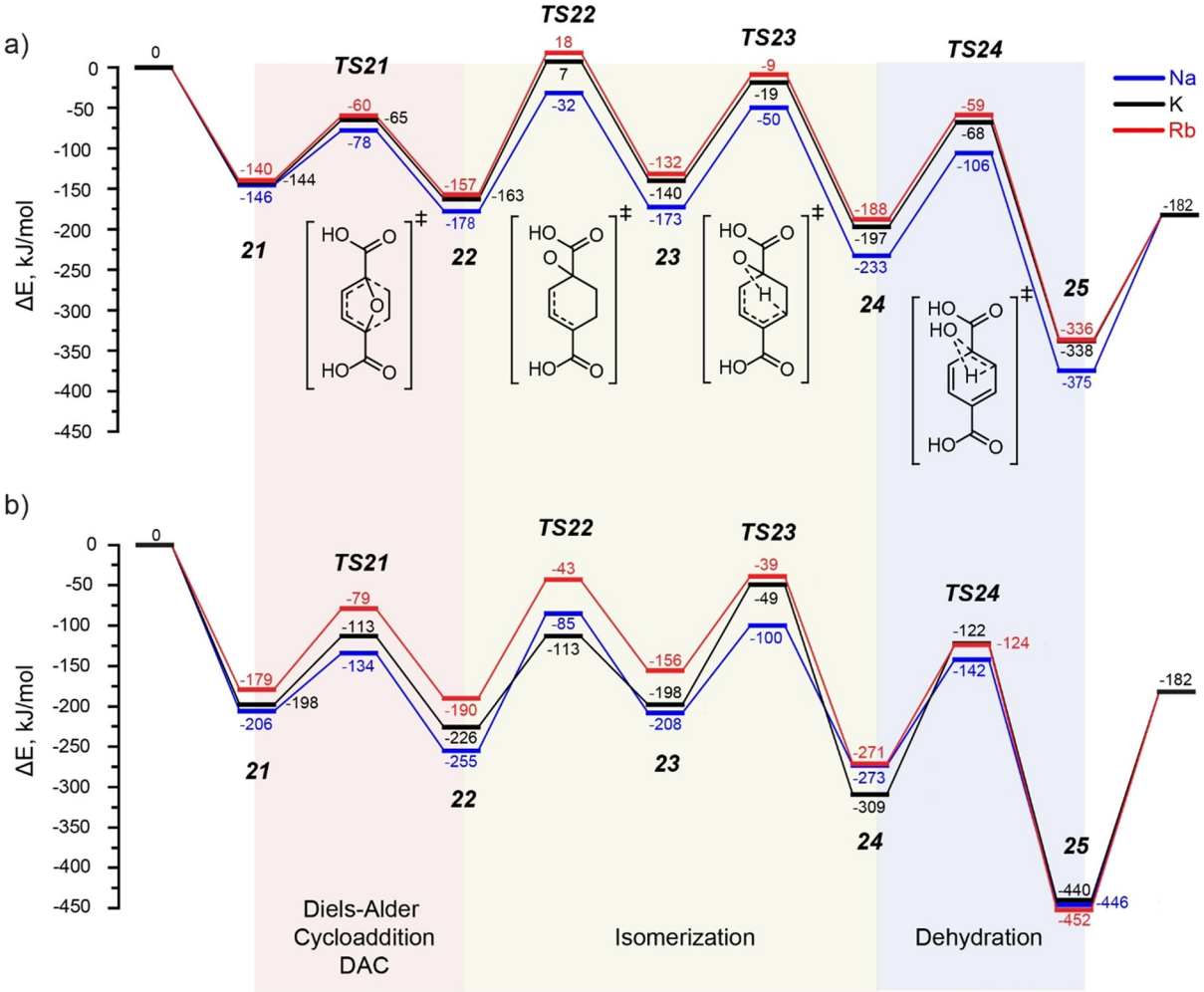

Figure 6. Energy diagrams of the DACD reaction of FDCA with ethylene yielding TPA, obtained with the periodic DFT calculations over a) the MFAU models and b) the MY models.

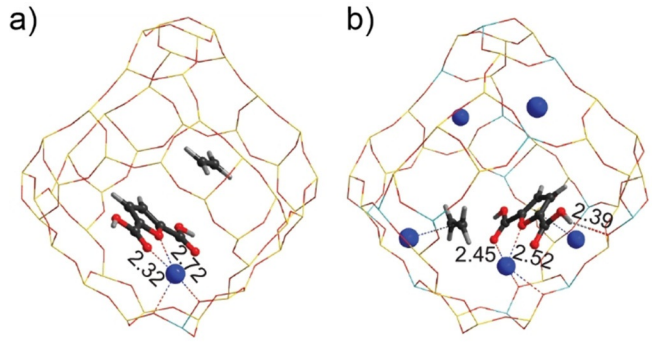

Figure 7. The optimized structures of the initial reactive states for FDCA coupling with ethylene (**21**) over a) NaFAU and b) NaY in dual-site adsorption mode. Selected interatomic distances are expressed in Å.

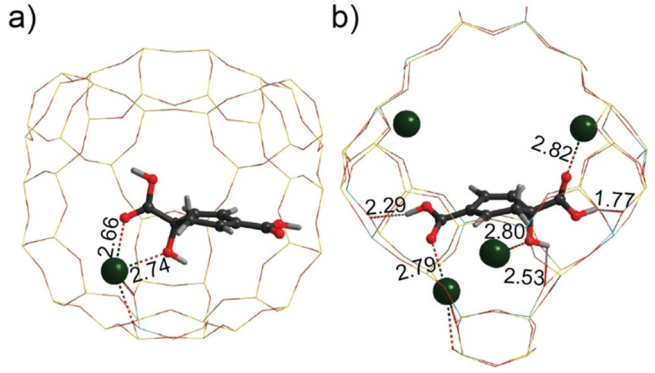

Figure 8. The optimized structures of the intermediate **24** in a) KFAU and b) KY models. Selected interatomic distances are expressed in Å.

figuration is the bidentate-coordinated FDCA without hydrogen bonding to the framework ($E_{ads} = -130$ kJ mol^{-1}). During all transformations of the DACD process, the reaction intermediates remain bound to the cation through the same two oxygen atoms. FDCA adsorbs nearly 2.5 times stronger than ethylene. The starting geometry **21**/MFAU is therefore represented by the η^2-adsorbed FDCA on the cation and ethylene interacting with the zeolite framework through van der Waals interactions (Figure 7a).

The coupling reaction (**21**→**22**) starts with ethylene approaching the adsorbed FDCA. The elementary reaction is most exothermic for NaFAU (−32 kJ mol^{-1}) and least for RbFAU (−17 kJ mol^{-1}). The activation energy for the DAC reaction is 68, 79 and 80 kJ mol^{-1} for NaFAU, KFAU and RbFAU, respectively. Despite the presence of strongly electron-withdrawing COOH moieties in FDCA, the reaction barriers are close to those of the more electron-rich diene 2,5-DMF.

For FDCA, a somewhat higher asymmetry of the transition state could be noted than for furan and 2,5-DMF because of the different starting configuration and the interaction mode of the substrate with the exchangeable sites. In **TS21**/MFAU the nascent C1–C6 bonds are more asymmetric with the longest nascent C4–C5 bond at the side of the exchangeable cation. The differences are 0.15, 0.03 and 0.02 Å for NaFAU, KFAU and RbFAU, respectively. Furthermore, the increasing cation size affects the interatomic distances between the cation and the two oxygen atoms in **21**/MFAU; that is, the $Na^+\cdots O_{carbonyl}$ distance (Figure 7) is 0.4 Å shorter than the $Na^+\cdots O_f$ distance. This difference does not exist for KFAU and is small for RbFAU (0.01 Å).

During the subsequent epoxide formation (**22**→**23**), both in NaFAU and KFAU, the cation–oxygen distances change. In **23**/MFAU, the $M^+\cdots O_{carbonyl}$ distance becomes longer. Only for RbFAU did we find a fully symmetric η^2-coordination of the epoxide. Formation of the epoxide is endothermic and the highest ΔE was computed for RbFAU (25 kJ mol^{-1}) and the smallest for NaFAU (5 kJ mol^{-1}). The reaction proceeds with activation barriers of 146, 170 and 175 kJ mol^{-1} for NaFAU, KFAU and RbFAU, respectively. Such activation energies are similar to those found for the DACD reactions of both furan and 2,5-DMF with ethylene over MFAU. Furthermore, the relative stabilities of **22**/MFAU, **TS22**/MFAU and **23**/MFAU increase only by approximately 10–23 kJ mol^{-1} relative to their counterparts in the one-pot DACD reaction of furan or 2,5-DMF with ethylene.

The subsequent alcohol formation (**23**→**24**) by intramolecular proton transfer from C5 to O_f is exothermic with ΔE values ranging from approximately −60 to −50 kJ mol^{-1} for NaFAU and RbFAU, respectively, and proceeds with practically equal barriers for all MFAU models (≈123 kJ mol^{-1}). Figure 8a shows a representative geometry of the **24**/KFAU product of this step. The invariance of the activation energy as a function of the cation radius is in contrast to the trends found for furan and 2,5-DMF substrates. Additionally, the state **24**/MFAU is approximately 23–40 kJ mol^{-1} more stable than **4**/MFAU and **14**/MFAU.

Finally, the dehydration takes place by proton transfer from C6 to the OH group resulting in elimination of water and the formation of TPA adduct **25**. Water remains coordinated to **25**, bound both to the framework and the cation. The only interaction between the cation and product **25** is maintained through the carbonyl oxygen atom. A significant amount of energy is gained in this step, which is consistent across the MFAU models (−148 to −141 kJ mol^{-1}). The barriers are also similar for all MFAUs (≈129 kJ mol^{-1}), unlike the situations encountered in the conversion of furan and 2,5-DMF. The presence of the carboxylic acid groups leads to an increased adsorption energy of **25**/MFAU by 30–50 kJ mol^{-1} compared to **5**/MFAU or **15**/MFAU. The total adsorption energy can reach a value of up to −375 kJ mol^{-1} for **25**/NaFAU. Such strong adsorption suggests the deactivation of the reactive MFAU environment. Upon formation, the oxygenated reaction intermediate **25** remains bound to the active site and renders the single-site MFAU catalyst inactive. Correspondingly, the desorption barriers of both FDCA and water combined are 193, 156 and 154 kJ mol^{-1} for NaFAU, KFAU and RbFAU, respectively. That is an increase of 7–21 kJ mol^{-1} with respect to the combined desorption barrier of *para*-xylene and water (**15**/MFAU).

The DFT results show that the first two reaction steps (**21**→**22**→**23**) in MFAU are qualitatively determined by the Lewis acidity of the cations. However, the last two reaction steps of the cycle (**23**→**24**→**25**) are independent of the cation. Al-

though the relative stabilities of the stationary points **24**/MFAU and **25**/MFAU follow the trend in Lewis acidity of the cations, the stabilities of the transition states correlate closely with the stabilities of the preceding intermediates making the reaction barriers invariant to the nature of the cation. We attribute this to the difference in the type of the elementary reaction. In the first two elementary steps, isomerization affects the position of the bridging O_f oxygen atom with respect to the cation. In the latter two elementary steps, the chemical transformations do not involve any change in bonding configuration of O_f with the cation.

2.4.2. Reaction over MY Catalysts

The combination of the various functional groups in FDCA and the presence of multiple accessible sites give rise to an increased number of adsorption geometries (Figure S1). These also included salt-like species, that is, deprotonated FDCA molecules coordinating to the alkali cations. The protons in such structures are bound to the basic oxygen atoms of the lattice. The preferred adsorption configuration ($E_{ads} = -148$ kJ mol^{-1}, NaY) is realized on the SII site (SII_{FDCA}) to which the FDCA binds in a η^5-fashion through its π system with two additional carboxylates moieties η^1-coordinated to the SIII site ($SIII_{FDCA}$; Figure 7b). For consistency, the starting configuration **21** contains ethylene co-adsorbed on the opposite SII site (SII_{C2}).

Similar to the conversion of the other furanic substrates studied in this work, the DAC reaction of FDCA with ethylene (**21**→**22**) is exothermic. The corresponding energy gain is smallest for RbY (−11 kJ mol^{-1}) and highest for NaY (−49 kJ mol^{-1}). The reaction proceeds with a barrier of 72, 85 and 100 kJ mol^{-1} for NaY, KY and RbY, respectively. The differences in bond length between the nascent C1–C6 and C4–C5 bonds were 0.04, 0.04 and 0.05 Å for NaY, KY and RbY, respectively. The hydrogen bonds between FDCA and the framework were not affected by the coupling reaction. All but the reaction barrier for RbY are close to those for the DAC reactions of both furan and 2,5-DMF with ethylene. However, considering the adsorption as a function of the cation Lewis acidity in **21**/MY, we suspect that the increased barrier arises from the adsorption effects caused by the increased number of electrostatic and hydrogen-bonding interactions rather than the electron-withdrawing nature of the carboxylic acid substituents.

The bicyclic intermediate **22** is then isomerized to epoxide **23**. This step is endothermic with the smallest ΔE computed for KY (28 kJ mol^{-1}) and the highest for NaY (47 kJ mol^{-1}). The reaction barriers are 170, 112 and 147 kJ mol^{-1} for NaY, KY and RbY respectively. The presence of multiple electrostatic interactions alters the reactivity trend compared to that found for the MFAU catalysts, that is, the NaY barrier increases by 24 kJ mol^{-1}, whereas those of KY and RbY are decreased by 57 and 28 kJ mol^{-1}, respectively. Furthermore, $\Delta\Delta E_{TS22}$ is significant in KY with 120 kJ mol^{-1}, versus 53 and 61 kJ mol^{-1} for NaY and RbY, respectively. Clearly, these changes arise from the manner in which the reaction intermediates dock onto the framework and cations. The reaction intermediates in this step can adopt the best adsorption geometry on K^+ ions due to them having the optimal cation radius: Na^+ is too small and Rb^+ is too large. If such a docking effect did not play the major role in the current case, we would probably have found a linear trend consistent with the Lewis acidity of the cations.

The second isomerization occurs by an intramolecular proton transfer from C5 to O_f leading to the formation of the alcohol **24**. The resulting OH group interacts with both the cation at the SII site and the basic framework. If proton transfer occurs, the carboxylic acid functionality close to the alcohol group rotates to coordinate a cation at another SII site (Figure 8b). This is an extra interaction that is not found in NaY and is only made possible by the size of the K^+ and Rb^+ ions. This makes the reaction **23**→**24** almost twice as exothermic for KY and RbY (−111 and −115 kJ mol^{-1}, respectively) compared to NaY (−65 kJ mol^{-1}). The activation barriers are 108, 149 and 117 kJ mol^{-1} for NaY, KY and RbY, respectively. Compared to the single-site models, these barriers either increase by 28 kJ mol^{-1} for KY or decrease by 15 kJ mol^{-1} for NaY relative to MFAU. Compared to **TS23**/MFAU, the stability of **TS23**/MY was increased by approximately 30–50 kJ mol^{-1}. A similar increase of the interaction strength was found for **23**/MY ranging from 24–58 kJ mol^{-1} relative to **23**/MFAU.

The dehydration step (**25** + H_2O) is highly exothermic with computed reaction energies ranging between 181 (RbY) to 131 kJ mol^{-1} (KY). The barriers are 131, 187 and 147 kJ mol^{-1} for NaY, KY and RbY respectively. Whereas the barrier for this reaction step in NaY is practically identical to that in NaFAU ($\approx$130 kJ mol^{-1}), the barrier in KY and RbY increased with 58 and 18 kJ mol^{-1}, respectively. The strongly increased barrier in KY originates from a large and increased interaction energy of **24** with the cations and framework in KY (Figure 8, $\Delta\Delta E_{24} =$ 112 kJ mol^{-1}). This is due to the formation of an extensive network of interactions, which even includes a carbonyl–cation interaction with a nearby SII site not belonging to the reactive cation ensemble initially used in **21**/KY. A similar geometry of **24** was also observed in RbY. However, the electrostatic interactions in this case are weaker and thus the barrier is increased only by 18 kJ mol^{-1}. Such geometry was not observed for either **4**/KY or **14**/KY.

Finally, the product **25** + H_2O was strongly adsorbed in the MY catalyst, with interaction energies of approximately −440 to −452 kJ mol^{-1}, which is qualitatively consistent with the computational findings for the MFAU catalyst. To desorb the reaction products, barriers of 264, 258 and 270 kJ mol^{-1} have to be overcome for NaY, KY and RbY, respectively. These barriers are approximately 70–120 kJ mol^{-1} higher than for their **25**/MFAU counterparts, and approximately 65–93 kJ mol^{-1} higher than for **15**/MY.

In summary, in the case of the FDCA substrate, we could not identify clear reactivity trends for the elementary reaction steps except the DAC reaction, for which we found a qualitatively similar trend for the MY models compared to that provided by MFAU. However, the barriers are similar except that found for RbY due to strong adsorption in the initial state of the DAC reaction. The presence of carboxylic acid functional groups causes a significant deviation from the linear reactivity trend found for the MFAU models, as they participate actively

in the interaction network established between the reaction intermediates and the cations and zeolite framework.

3. Conclusions

Analysis of the reaction cycles described here indicates that the presence of multiple accessible sites in the confined microporous space of faujasite zeolites alters the reactivity trends significantly compared to those predicted with the isolated-site model. For the high-silica model containing only a single-site cation site for adsorption and reaction, the reactivity is determined by the Lewis acidity of the cation. In contrast, if a low-silica model is used, the possibility of cooperative interactions between the zeolite matrix and accessible cations with the reactants lowers the reaction barriers. Overall, the reactivity is not determined by only the Lewis acidity, but also by the geometrical constraints imposed by the size of the cations and the reactants. For instance, the DAC reactivity trend of all but the reaction between FDCA and ethylene is reversed in the MY models compared to the trend expected from the difference in Lewis acidity of the exchangeable cations. The reactivity trends in the confined spaces of faujasite zeolites cannot be ascribed to the intrinsic electronic properties of the substrates or catalytic Lewis acid sites. The analysis of the computed reaction energetics and optimized geometries suggests that the overall DAC barriers in MY are determined mostly by the geometrical fit of the furan derivative to the SII and SIII active sites. This is reminiscent of the induced-fit model in enzyme catalysis.[55,56]

The presence of electron-donor or acceptor substituents on the furan ring does not have a direct effect on the DACD reactivity. The computed barriers are influenced by steric effects and the strength of the interactions within the zeolite cage. The stability of all reactive species increases due to interactions with both the Lewis acidic extra-framework sites and Lewis basic framework.[57–59] The existence of a network of multiple noncovalent interactions capable of aligning and stabilizing reaction intermediates is usually referred to as molecular recognition.[60] For the current system they lead to a strong decrease of the isomerization and dehydration barriers so that, a priori, the respective steps cannot be considered rate-limiting. It is such molecular recognition features that limit the reactivity of oxygenated substrates such as FDCA rather than the presence of electron-withdrawing substituents. Indeed, the strong multiple-site binding of FDCA gives rise to high adsorption energies for this substrate and its derivatives. For instance, the alcohol intermediate **25** is approximately 100 kJ mol^{-1} more stable inside the Y-zeolite pores than its furan-derived counterpart **5**, rendering it as a dormant state rather than a catalytic intermediate.

Furthermore, we note that the stabilization of transition states in the MY models is aided by the relocation of the cations, most notably that of the cation at the SIII site (for example **TS2**/NaY and **24**/KY). Such adsorption-induced migration of exchangeable cations has previously been observed experimentally[61,62] and in molecular dynamics simulations.[63,64] It is driven by the formation of a more energetically favorable interaction with the substrate. In our calculations, the substantial displacement of the exchangeable cations was observed as a result of the cooperative binding of the adsorbent by multiple cations, but it was not captured by the isolated-site models.

In conclusion, we performed a mechanistic study on the DACD reactions of furan, 2,5-DMF and FDCA with ethylene to form benzene, *para*-xylene and TPA, respectively. By studying these three reactions computationally using chemically representative low-silica alkali-metal-exchanged faujasite models, we show that single-site zeolite models cannot capture the key features of molecular recognition and confinement present in such materials. Mechanistic proposals based on such models can thus be inadequate to either qualitatively explain or predict (expected) experimental reactivity trends. Catalytic reactivity often arises from a complex network of multiple interactions between the catalyst and the reactive intermediate. Predictions about qualitative catalytic trends based on reductionist single-site models should thus be evaluated with great care.

Experimental Section

All calculations were carried out within the framework of density functional theory (DFT) with PBE exchange-correlation functional,[65] as implemented in the Vienna Ab Initio Simulation Package (VASP).[66–70] The electronic wavefunctions were expanded following the projected-augmented-wave (PAW) scheme to describe the electron–ion interactions. Long-range dispersive interactions were accounted for by using the DFT-D3 method with Becke–Johnson damping.[71,72] The k-point mesh was restricted to the gamma point. The total energies were computed with a cut-off energy of 500 eV and a root-mean-square (RMS) force convergence criterion of 0.015 eV Å^{-1}. Sometimes, a model did not fully achieve the desired RMS force criterion. On those occasions, the convergence criterion was relaxed to 0.035 eV Å^{-1}. Careful checks of the forces and geometries showed that this effect was typically due to excess forces on cations confined within double six-membered rings distant from the reaction site. Extensive computational tests revealed that the current zeolite models feature extremely shallow potential energy surfaces with numerous degrees of freedom. Structural optimization below 0.05 eV Å^{-1} was therefore usually accompanied by energy changes not greater than 5 kJ mol^{-1}. Nevertheless, low RMS forces on the optimized structures were typically desired for an accurate vibrational analysis.

The models were based on the rhombohedral unit cell of the faujasite zeolite containing 48 T sites and 96 oxygen atoms. The high-silica model (Si/Al = 47, $Si_{47}Al_1O_{96}M_1$) was characterized by one isolated site per rhombohedral unit cell. Na^+, K^+ or Rb^+ cations (M) compensated the charge induced by the aluminum substitution. The low-silica model (Si/Al = 2.4, $Si_{34}Al_{14}O_{96}M_{14}$) was characterized by a high active-site density. Each model only contained one type of each cation. More information about both cation placement based on experimental data and lattice relaxations can be found in the Supporting Information.

To identify the transition state a two-step approach was adopted. First, a climbing nudged elastic band (CNEB) calculation[73,74] was performed to estimate the minimum energy pathway from the initial state to the final state (5 eV Å^{-2} spring constant, maximum length hypervector between images 0.5 Å). The accepted RMS force of the converged CNEB was 0.14 eV Å^{-1} or lower. After this, the second step of our optimization procedure was started, which consisted of a geometry optimization of the identified transition state using the quasi-Newton procedure (maximum RMS

< 0.015 eV Å^{-1}). Frequencies were then calculated with the finite displacement method (0.0015 Å) to confirm the validity of the found transition states. A characteristic high imaginary frequency corresponding to the reaction coordinate that was not present in either the initial state or finals state was always found in the transition-state structures.

Acknowledgements

This work was supported by the Netherlands Center for Multiscale Catalytic Energy Conversion (MCEC), an NWO Gravitation program funded by the Ministry of Education, Culture and Science of the government of the Netherlands. E.A.P. thanks the Government of the Russian Federation (grant 074-U01) and the Ministry of Education and Science of the Russian Federation (project 11.1706.2017/4.6) for support. The authors thank The Netherlands Organization for Scientific Research (NWO) for access to the national high-performance computing facilities.

Conflict of Interest

The authors declare no conflict of interest.

Keywords: ab initio calculations · cooperativity · molecular recognition · reaction mechanisms · zeolites

[1] L. B. McCusker, C. Baerlocher, *Stud. Surf. Sci. Catal.* **2005**, *157*, 41 – 64.
[2] T. Ennaert, J. Van Aelst, J. Dijkmans, R. De Clercq, W. Schutyser, M. Dusselier, D. Verboekend, B. F. Sels, *Chem. Soc. Rev.* **2016**, *45*, 584 – 611.
[3] R. A. Schoonheydt, P. Geerlings, E. A. Pidko, R. A. van Santen, *J. Mater. Chem.* **2012**, *22*, 18705 – 18717.
[4] D. R. Rolison, C. A. Bessel, *Acc. Chem. Res.* **2000**, *33*, 737 – 744.
[5] E. M. Gallego, M. T. Portilla, C. Paris, A. León-Escamilla, M. Boronat, M. Moliner, A. Corma, *Science* **2017**, *355*, 1051 – 1054.
[6] B. Smit, T. L. M. Maesen, *Nature* **2008**, *451*, 671 – 678.
[7] B. C. Bukowski, J. Greeley, *J. Phys. Chem. C* **2016**, *120*, 6714 – 6722.
[8] S. Siahrostami, H. Falsig, P. Beato, P. G. Moses, J. K. Nørskov, F. Studt, *ChemCatChem* **2016**, *8*, 767 – 772.
[9] C.-M. Wang, R. Y. Brogaard, Z.-K. Xie, F. Studt, *Catal. Sci. Technol.* **2015**, *5*, 2814 – 2820.
[10] G. Jones, T. Bligaard, F. Abild-Pedersen, J. K. Nørskov, *J. Phys. Condens. Matter* **2008**, *20*, 064239.
[11] S. Wang, V. Petzold, V. Tripkovic, J. Kleis, J. G. Howalt, E. Skúlason, E. M. Fernández, B. Hvolbæk, G. Jones, A. Toftelund, H. Falsig, M. Björketun, F. Studt, F. Abild-Pedersen, J. Rossmeisl, J. K. Nørskov, T. Bligaard, *Phys. Chem. Chem. Phys.* **2011**, *13*, 20760.
[12] J. A. Melero, J. Iglesias, A. Garcia, *Energy Environ. Sci.* **2012**, *5*, 7393.
[13] G. W. Huber, A. Corma, *Angew. Chem. Int. Ed.* **2007**, *46*, 7184 – 7201; *Angew. Chem.* **2007**, *119*, 7320 – 7338.
[14] C.-H. Zhou, X. Xia, C.-X. Lin, D.-S. Tong, J. Beltramini, *Chem. Soc. Rev.* **2011**, *40*, 5588 – 5617.
[15] Y. Román-Leshkov, M. E. Davis, *ACS Catal.* **2011**, *1*, 1566 – 1580.
[16] H. O. Folkins in *Ullmann's Encyclopedia of Industrial Chemistry*, Wiley-VCH, Weinheim, **2000**, pp. 41 – 93.
[17] X. Huang, T. I. Korányi, M. D. Boot, E. J. M. Hensen, *Green Chem.* **2015**, *17*, 4941 – 4950.
[18] P. J. Deuss, M. Scott, F. Tran, N. J. Westwood, J. G. De Vries, K. Barta, *J. Am. Chem. Soc.* **2015**, *137*, 7456 – 7467.
[19] R. Rinaldi, R. Jastrzebski, M. T. Clough, J. Ralph, M. Kennema, P. C. A. Bruijnincx, B. M. Weckhuysen, *Angew. Chem. Int. Ed.* **2016**, *55*, 8164 – 8215; *Angew. Chem.* **2016**, *128*, 8296 – 8354.
[20] B. Güvenatam, E. H. J. Heeres, E. A. Pidko, E. J. M. Hensen, *Catal. Today* **2016**, *259*, 460 – 466.
[21] B. Güvenatam, E. H. J. Heeres, E. A. Pidko, E. J. M. Hensen, *Catal. Today* **2016**, *269*, 9 – 20.
[22] P. Ferrini, C. Chesi, N. Parkin, R. Rinaldi, *Faraday Discuss.* **2017**, *202*, 403 – 413.
[23] A. Corma Canos, S. Iborra, A. Velty, *Chem. Rev.* **2007**, *107*, 2411 – 2502.
[24] Y. Nakagawa, M. Tamura, K. Tomishige, *ACS Catal.* **2013**, *3*, 2655 – 2668.
[25] M. Besson, P. Gallezot, C. Pinel, *Chem. Rev.* **2014**, *114*, 1827 – 1870.
[26] J. N. Chheda, G. W. Huber, J. A. Dumesic, *Angew. Chem. Int. Ed.* **2007**, *46*, 7164 – 7183; *Angew. Chem.* **2007**, *119*, 7298 – 7318.
[27] C. O. Kappe, S. S. Murphree, A. Padwa, *Tetrahedron* **1997**, *53*, 14179 – 14233.
[28] A. E. Settle, L. Berstis, N. A. Rorrer, Y. Roman-Leshkóv, G. T. Beckham, R. M. Richards, D. R. Vardon, *Green Chem.* **2017**, *19*, 3468 – 3492.
[29] J. Howell, J. D. Goddard, W. Tam, *Tetrahedron* **2009**, *65*, 4562 – 4568.
[30] M. Lautens, K. Fagnou, S. Hiebert, *Acc. Chem. Res.* **2003**, *36*, 48 – 58.
[31] J. Fabri, U. Graeser, T. A. Simo, *Ullmann's Encycl. Ind. Chem.*, Wiley-VCH, Weinheim, 2000, pp. 643 – 664
[32] D. I. Collias, A. M. Harris, V. Nagpal, I. W. Cottrell, M. W. Schultheis, *Ind. Biotechnol.* **2014**, *10*, 91 – 105.
[33] P. T. M. Do, J. R. McAtee, D. A. Watson, R. F. Lobo, *ACS Catal.* **2013**, *3*, 41 – 46.
[34] R. E. Patet, N. Nikbin, C. L. Williams, S. K. Green, C.-C. Chang, W. Fan, S. Caratzoulas, P. J. Dauenhauer, D. G. Vlachos, *ACS Catal.* **2015**, *5*, 2367 – 2375.
[35] C. L. Williams, K. P. Vinter, C.-C. Chang, R. Xiong, S. K. Green, S. I. Sandler, D. G. Vlachos, W. Fan, P. J. Dauenhauer, *Catal. Sci. Technol.* **2016**, *6*, 178 – 187.
[36] C.-C. Chang, H. J. Cho, J. Yu, R. J. Gorte, J. Gulbinski, P. Dauenhauer, W. Fan, *Green Chem.* **2016**, *18*, 1368 – 1376.
[37] Y. P. Wijaya, I. Kristianto, H. Lee, J. Jae, *Fuel* **2016**, *182*, 588 – 596.
[38] I. F. Teixeira, B. T. W. Lo, P. Kostetskyy, M. Stamatakis, L. Ye, C. C. Tang, G. Mpourmpakis, S. C. E. Tsang, *Angew. Chem. Int. Ed.* **2016**, *55*, 13061 – 13066; *Angew. Chem.* **2016**, *128*, 13255 – 13260.
[39] A. Zheng, Z. Zhao, S. Chang, Z. Huang, K. Zhao, H. Wu, X. Wang, F. He, H. Li, *Green Chem.* **2014**, *16*, 2580 – 2586.
[40] E. Mahmoud, J. Yu, R. J. Gorte, R. F. Lobo, *ACS Catal.* **2015**, *5*, 6946 – 6955.
[41] J. J. Pacheco, M. E. Davis, *Proc. Natl. Acad. Sci. USA* **2014**, *111*, 8363 – 8367.
[42] C. L. Williams, C. Chang, P. Do, N. Nikbin, S. Caratzoulas, D. G. Vlachos, R. F. Lobo, W. Fan, P. J. Dauenhauer, *ACS Catal.* **2012**, *2*, 935 – 939.
[43] S. K. Green, R. E. Patet, N. Nikbin, C. L. Williams, C. C. Chang, J. Yu, R. J. Gorte, S. Caratzoulas, W. Fan, D. G. Vlachos, P. J. Dauenhauer, *Appl. Catal. B* **2016**, *180*, 487 – 496.
[44] Y.-P. Li, M. Head-Gordon, A. T. Bell, *J. Phys. Chem. C* **2014**, *118*, 22090 – 22095.
[45] Y.-P. Li, M. Head-Gordon, A. T. Bell, *ACS Catal.* **2016**, *6*, 5052 – 5061.
[46] N. Nikbin, P. T. Do, S. Caratzoulas, R. F. Lobo, P. J. Dauenhauer, D. G. Vlachos, *J. Catal.* **2013**, *297*, 35 – 43.
[47] Y. R. Rohling, E. Uslamin, B. Zijlstra, I. C. Tranca, I. A. W. Filot, E. J. M. Hensen, E. A. Pidko, *ACS Catal.* **2017**, https://doi.org/10.1021/acscatal.7b03343.
[48] N. Rai, S. Caratzoulas, D. G. Vlachos, *ACS Catal.* **2013**, *3*, 2294 – 2298.
[49] J. Dijkmans, M. Dusselier, W. Janssens, M. Trekels, A. Vantomme, E. Breynaert, C. Kirschhock, B. F. Sels, *ACS Catal.* **2016**, *6*, 31 – 46.
[50] G. Yang, E. A. Pidko, E. J. M. Hensen, *ChemSusChem* **2013**, *6*, 1688 – 1696.
[51] G. Li, E. A. Pidko, E. J. M. Hensen, *Catal. Sci. Technol.* **2014**, *4*, 2241 – 2250.
[52] N. Nikbin, S. Feng, S. Caratzoulas, D. G. Vlachos, *J. Phys. Chem. C* **2014**, *118*, 24415 – 24424.
[53] T. Frising, P. Leflaive, *Microporous Mesoporous Mater.* **2008**, *114*, 27 – 63.
[54] S. M. Payne, F. M. Kerton, *Green Chem.* **2010**, *12*, 1648 – 1653.
[55] D. E. Koshland, *Angew. Chem. Int. Ed. Engl.* **1995**, *33*, 2375 – 2378; *Angew. Chem.* **1994**, *106*, 2468 – 2472.
[56] S. J. Benkovic, *Science* **2003**, *301*, 1196 – 1202.
[57] P. Mignon, E. A. Pidko, R. A. Van Santen, P. Geerlings, R. A. Schoonheydt, *Chem. Eur. J.* **2008**, *14*, 5168 – 5177.
[58] K. S. Walton, M. B. Abney, M. D. LeVan, *Microporous Mesoporous Mater.* **2006**, *91*, 78 – 84.
[59] P. Nachtigall, M. R. Delgado, D. Nachtigallova, C. O. Arean, *Phys. Chem. Chem. Phys.* **2012**, *14*, 1552 – 1569.

[60] E. Persch, O. Dumele, F. Diederich, *Angew. Chem. Int. Ed.* **2015**, *54*, 3290 – 3327; *Angew. Chem.* **2015**, *127*, 3341 – 3382.
[61] A. Nicolas, S. Devautour-Vinot, G. Maurin, J. C. Giuntini, F. Henn, *J. Phys. Chem. C* **2007**, *111*, 4722 – 4726.
[62] U. Simon, M.. Franke, *Microporous Mesoporous Mater.* **2000**, *41*, 1 – 36.
[63] C. Abrioux, B. Coasne, G. Maurin, F. Henn, M. Jeffroy, A. Boutin, *J. Phys. Chem. C* **2009**, *113*, 10696 – 10705.
[64] G. Maurin, D. F. Plant, F. Henn, R. G. Bell, *J. Phys. Chem. B* **2006**, *110*, 18447 – 18454.
[65] B. K. Perdew, J. P. M. Ernzerhof, *Phys. Rev. Lett.* **1996**, *77*, 3865 – 3868.
[66] G. Kresse, J. Hafner, *Phys. Rev. B* **1994**, *49*, 14251 – 14269.
[67] G. Kresse, J. Furthmüller, *Phys. Rev. B* **1996**, *54*, 11169 – 11186.
[68] G. Kresse, J. Furthmüller, *Comput. Mater. Sci.* **1996**, *6*, 15 – 50.
[69] G. Kresse, D. Joubert, *Phys. Rev. B* **1999**, *59*, 1758 – 1775.
[70] G. Kresse, J. Hafner, *Phys. Rev. B* **1993**, *47*, 558 – 561.
[71] S. Grimme, J. Antony, S. Ehrlich, H. Krieg, *J. Chem. Phys.* **2010**, *132*, 154104.
[72] S. Grimme, S. Ehrlich, L. Goerigk, *J. Comput. Chem.* **2011**, *32*, 1456 – 1465.
[73] G. Henkelman, B. P. Uberuaga, H. Jónsson, *J. Chem. Phys.* **2000**, *113*, 9901 – 9904.
[74] G. Henkelman, H. Jónsson, *J. Chem. Phys.* **2000**, *113*, 9978 – 9985.

Manuscript received: September 27, 2017
Revised manuscript received: November 3, 2017
Accepted manuscript online: November 3, 2017
Version of record online: December 13, 2017

